Catalysis Today 172 (2011) 58–65

Contents lists available at ScienceDirect

Catalysis Today

journal homepage: www.elsevier.com/locate/cattod

MCM-41-based materials for the photo-catalytic degradation of Acid Orange 7

V. Elías[a,d], E. Vaschetto[a,d], K. Sapag[b,c], M. Oliva[c,d], S. Casuscelli[a,d], G. Eimer[a,d,*]

[a] CITeQ-Universidad Tecnológica Nacional-Facultad Regional Córdoba, Maestro López esq. Cruz Roja Argentina, 5016 Córdoba, Argentina
[b] INFAP-Universidad Nacional de San Luis, San Luis, Argentina
[c] FaMAF-Universidad Nacional de Córdoba, Córdoba, Argentina
[d] CONICET, Argentina

ARTICLE INFO

Article history:
Received 19 November 2010
Received in revised form 29 April 2011
Accepted 5 May 2011
Available online 12 June 2011

Keywords:
Heterogeneous photocatalysis
Transition metals
Titania
Visible radiation
Mesoporous materials
Azo-dye

ABSTRACT

MCM-41 materials were modified with Cr, Fe, Co and Ti and characterized by ICP, XRD, N_2 adsorption, UV–Vis DRS and TPR. Their photo-catalytic activity was evaluated for the degradation of Acid Orange 7 (AO7) in aqueous suspensions irradiated by artificial UV–Vis and visible light. The results showed that the Cr-modified catalysts exhibited the highest activity under visible light. The presence of Cr^{6+} highly dispersed on the internal surface of the MCM-41 structure would have a significant influence on the photo-activity. Thus, the lack of a notable increment in the activity when the Cr loading was duplicated is probably due to the increased presence of inactive Cr^{3+} species. Upon the TiO_2 loading, an increase in the degradation was not observed. It is suggested that the Cr^{3+} species, as Cr_2O_3 clusters and/or α-Cr_2O_3 nano-particles, could avoid the desired heterojunction between Cr^{6+} and titania species.

1. Introduction

Since 60′decade, different countries around the world have understood the importance of conjugate the enrichment of the economies of countries with the preservation of the environment. Thus emerges the called "sustainable development" and the countries that belong to ONU have assumed several commitments to conciliate their economics activities with environmental protection. One of the most important natural resources is the water. This substance cannot be considered since a commercial point of view because is fundamental to the human life development. Therefore, sustainable development polices would imply the adoption of regulations for the correct use and preservation of water resources. Taking into account the industrial activities, we have to consider that organic dyes constitute one of the larger groups of pollutants in wastewater released from textile industries. The release of colored wastewaters in the ecosystem is a dramatic source of esthetic pollution, eutrophication, and perturbations in aquatic life. Most of synthetic dyes are azo-dyes that are carcinogenic, mutagenic and toxic substances. Moreover, their molecules are hardly degradable and resist the conventional chemical and biological treatments [1,2]. In this context, among the new oxidation methods called "advanced oxidation processes" (AOP), heterogeneous photo-catalysis appears as an emerging and cost effective, destructive technology that leads to the total mineralization of many organic pollutants [3]. Many research groups have been focused on this last treatment, suggesting that the photo-sensitized degradation on semiconductor surfaces can have efficient applications for the remediation of colored organic pollutants present in textile dyestuffs [4–7]. Commercial TiO_2 (Degussa P-25) is one of the most popular semiconductor used as photo-catalyst, because it is stable and inexpensive, besides good results have been reached in organic compounds degradation with their use [5,8–10]; nevertheless, it requires UV light (<400 nm) to be excited and become capable of photo-oxidation [11]. To improve the performance of conventional photo-catalytic reactions it should be taken into account some important limitations that affect the process development: (1) the use of UV light that is expensive because requires additional sources of energy and it is also harmful to living species; (2) the low surface area of TiO_2 particles ($50 \pm 15\ m^2/g$) that besides, when they are used in suspension tends to form aggregates which provokes a higher decrease in the surface area affecting the process efficiency; and (3) the small size of the TiO_2 particles that does not facilitate their recovery from the effluent wastewater. With the aim of get over these limitations, materials with efficiencies similar to anatase, but that possess spectral properties more closely adapted to the solar spectrum, have been developed. Thus, an interesting approach to deal with the issue of extending the response of the photo-catalyst toward the visible spectral region is the use of

* Corresponding author at: CITeQ-Universidad Tecnológica Nacional-Facultad Regional Córdoba, Maestro López esq. Cruz Roja Argentina, 5016 Córdoba, Argentina.
E-mail address: geimer@scdt.frc.utn.edu.ar (G. Eimer).

0920-5861/$ – see front matter © 2011 Elsevier B.V. All rights reserved.
doi:10.1016/j.cattod.2011.05.003

different transition metals [12–14]. About the subject, several reports about the incorporation of highly dispersed transition metal ions (Cr, Fe, Co) into titania have been made [12,13,15]. On the other hand, the problem about the separation of the catalyst from the treated water has been solved by fixing the catalyst on a support like silica gel, quartz optical fibers, glass fibers, ceramics, cellulose membranes, polymer films, zeolites, etc. [16]. In this context, there are many reports involving the modification of porous adsorbents with transition metals to be used as photo-catalysts [11]. MCM-41 mesoporous molecular sieves are excellent candidates to be modified by the loading of several transition metal oxides due to their interesting physical properties that include a high specific surface area of about 1000 m^2/g and a specific pore volume of around 1 mL/g [17]. Thus, the mesoporous structure of the MCM-41 materials allows a high dispersion of the photo-catalytic active species, immobilizing them onto the surface of a suitable solid inert material [11,18–26]. Therefore, a photo-catalyst capable to be activated with visible radiation, with high surface areas and easy recovery from the aqueous suspensions can be developed. In this sense, the synthesis of TiO_2-loaded transition metal modified MCM-41 has been reported as good catalyst for the degradation of phenolic compounds under visible light [18].

Bearing in mind the previous discussion, the scope of the present work is to study the photo-catalytic activity of MCM-41 mesoporous materials modified with two different loadings of chromium, iron and cobalt and then loaded with TiO_2.The synthesized materials were tested in the photo-degradation of Acid Orange 7 (AO7), chosen as a dye probe molecule, under artificial visible light. For comparison, the degradation tests were also conducted under UV–Vis light.

2. Experimental procedures

2.1. Synthesis

The metal-free MCM-41 mesoporous molecular sieve was synthesized as previously reported [27] following the method B, using cetyltrimethylammonium bromide (CTAB) (Merck 99%) as template and tetraethoxysilane (TEOS) (Aldrich 98%) as silicon source. The synthesis mixture (pH 11.25) was stirred at room temperature for 4 h. Then, this gel was heated at 70 °C under stirring in a closed flask. The MCM-41 host, previously calcined for 5 h in oven at 500 °C, was modified with transition metals by the wet impregnation method. Two different concentrations of the precursor aqueous solution ($Cr(NO_3)_3{\cdot}9H_2O$ (Anedra 98%), $Fe(NO_3)_3{\cdot}9H_2O$ (Aldrich 98%) or $Co(NO_3)_2{\cdot}6H_2O$ (Riedel-de Haën 98%) were used to reach a loading of around 5 and 10 wt% and the pH of the these solutions was approximately 5. The MCM-41 host (0.75 g) was dispersed in the precursor solution at room temperature and then, the solvent (water) was slowly removed by rotary evaporation at 50 °C for 30 min. The resulting powder was dried at 60 °C and calcined for 9 h at 500 °C. The materials were named: TM/MCM-41(5) or TM/MCM-41(10), where TM indicates the used transition metal (Cr, Fe or Co) and the expected percentages of the metal loading are indicated in parentheses. Then, these catalysts were loaded with titania by the same procedure used for the other metals, dispersing 0.75 g of the solid in a 3.2 wt.% solution of titanium *n*-butoxide (Fluka 97%) in isopropanol (Cicarelli 99.5%). The materials were named: TiO_2/TM/MCM-41(5) and TiO_2/TM/MCM-41(10). For comparative purposes the TiO_2/MCM-41 was also synthesized.

2.2. Characterization

The (XRD) X-ray diffraction patterns were recorded in a Philips PW 3830 diffractometer with Cu Kα radiation (λ = 1.5418 Å) in the range of 2θ from 1.5° to 7° and from 20° to 80°. A profile fitting was made to each maximum in the high angle range, and the mean crystallite size $\langle D\rangle$ of the corresponding phase was estimated using the Scherrer formulae: $\langle D\rangle = 0.9\lambda/\beta\cos\theta$, where β (in radians) is the peak intrinsic breadth after subtraction of the instrumental contribution, λ is the X-ray wavelength and θ is the Bragg angle [28]. It is worth to note that the Scherrer equation was used in order to perform a rough estimation of the crystallite size. UV–Vis diffuse reflectance spectra (UV–Vis DRS) in absorbance mode were recorded using an Optronics OL 750–427 spectrometer in the wavelength range of 200–900 nm. The Cr, Fe and Co content was determined by Atomic Absorption spectroscopy (AA) using a Varian SpectrAA 220 and Ti content by Inductively Coupled Plasma Atomic Emission Spectroscopy (ICP-AES) using a Thermo Fisher XSeries II. The specific surface area, the pore size distribution and the total pore volume were determined from N_2 adsorption–desorption isotherms obtained at −196 °C using a Micromeritics ASAP 2010. The surface area was determined by the Brunauer–Emmett–Teller (BET) method in the pressure range of P/P_0: 0.01–0.25. The pore size distributions were determined by the Barrett–Joyner–Halenda (BJH) method, based on the Kelvin equation [29]. The reducibility of the catalysts was measured by Temperature-programmed reduction (TPR) experiments in a Quantachrome Chembet 3000. In these experiments, the samples were heated at a rate of 10 °C/min in the presence of H_2 (5% H_2/N_2 flow, 20 mL/min STP), and the reduction reaction was monitored by the H_2 consumption.

2.3. Catalytic experiments

The degradation experiments were performed with a photo-reactor, which consisted of a borosilicate glass tube of 0.85 L capacity with a sintered glass piece placed at the bottom and four UV–Vis lamps (Actinic BL 20 W, Philips) placed around the tube. These lamps emit a continuum spectrum in the wavelength range between 350 and 400 nm and two bands at 404 and 438 nm. To avoid the radiation scattering, an aluminum foil was placed around the photo-reactor. For temperature control, a tube was placed in the center of the reactor allowing the circulation of refrigeration water. A circulation pump and a thermostated water bath (20 ± 0.2 °C) were used for this purpose. For the photo-catalytic tests with visible light one needs assure that only this radiation reaches the catalyst suspension. This is the reason why an acrylic filter of 4 mm thick was placed between the lamps and the glass tube with the aim of excluding UV radiation. The transmission spectrum of the filter exhibits a sharp decrease under 400 nm, thus effectively eliminating the most of UV radiation of the lamp emission. Therefore, the two bands of the lamp available for the reaction are at 404 and 438 nm. It is important to take into account that approximately a 10% of the lamp radiation reaches the reactor when the filter is placed. The suspension volume employed in all of the experiments was 0.5 L with an initial concentration of the AO7 (Aldrich >85%) and the catalyst of 20 ppm (57 μM) and 1 g/L, respectively. Prior to each reaction, the catalyst is calcined at 500 °C. The suspended catalyst in aqueous system was oxygenated using an air flow of 1 L/min, which allowed reach a percentage of oxygen saturation of around 90%. The measured pH of the suspension was of 5. Prior to irradiation, the suspension was stirred in the dark under air flow for 45 min in order to reach the adsorption/desorption equilibrium. After the adsorption period, an initial sample was extracted to calculate the initial concentration (C_0) and then, the experimental run starts. Samples of 10 mL were collected each one hour and filtered. The concentration (C) of AO7 was monitored by measuring the absorbance at λ = 485 nm using Jasco 7800 spectrophotometer. The degradation percentage was calculated as $X = (C_0 - C) \times 100/C_0$.

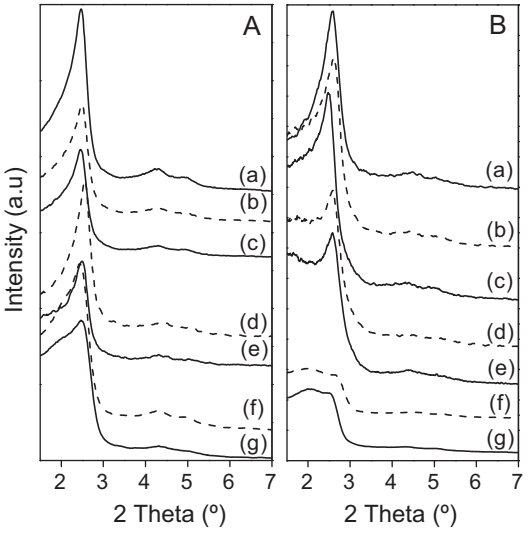

Fig. 1. Low-angle XRD patterns of (A) – (a) MCM-41, (b) Cr/MCM-41(5), (c) Cr/MCM-41(10), (d) Fe/MCM-41(5), (e) Fe/MCM-41(10), (f) Co/MCM-41(5), (g) Co/MCM-41(10); (B) – (a) TiO_2/MCM-41, (b) TiO_2/Cr/MCM-41(5), (c) TiO_2/Cr/MCM-41(10), (d) TiO_2/Fe/MCM-41(5), (e) TiO_2/Fe/MCM-41(10), (f) TiO_2/Co/MCM-41(5), (g) TiO_2/Co/MCM-41(10).

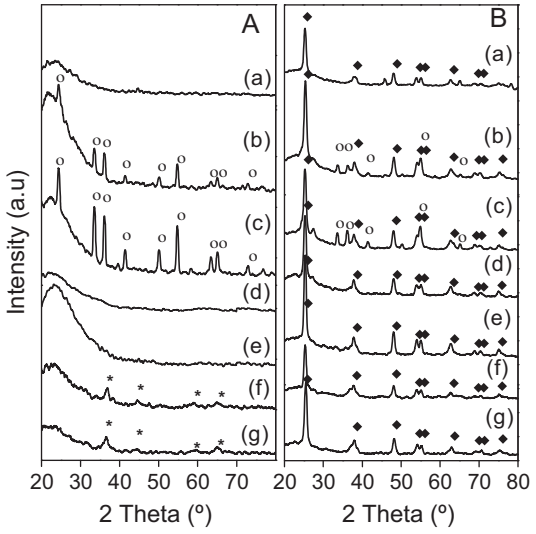

Fig. 2. High-angle XRD patterns of (A) – (a) MCM-41, (b) Cr/MCM-41(5), (c) Cr/MCM-41(10), (d) Fe/MCM-41(5), (e) Fe/MCM-41(10), (f) Co/MCM-41(5), (g) Co/MCM-41(10); (B) (a) TiO_2/MCM-41, (b) TiO_2/Cr/MCM-41(5), (c) TiO_2/Cr/MCM-41(10), (d) TiO_2/Fe/MCM-41(5), (e) TiO_2/Fe/MCM-41(10), (f) TiO_2/Co/MCM-41(5), (g) TiO_2/Co/MCM-41(10). (○) Cr_2O_3, (*) Co_3O_4 and (♦) TiO_2 (anatase).

3. Results and discussion

3.1. Synthesis and characterization of the catalyst

Table 1 summarizes the chemical composition and the textural and structural properties of the calcined catalysts and Fig. 1 gives out the corresponding low-angle XRD patterns. The XRD pattern of the calcined sample MCM-41 (Fig. 1A) showed the reflections (1 0 0), (1 1 0) and (2 0 0) which are typical of mesoporous MCM-41 structure with a hexagonal array of uni-dimensional pores [30]. Although some modifications in the diffraction pattern were observed for the TM-modified samples, even in the case of the catalysts with the highest TM loading, the three diffractions lines are still observed. This fact indicates that the mesoporous structure of the support was remained during the impregnation and calcination process. The additional loading of TiO_2 has not greatly modified the structural ordering of the samples, except for the TiO_2/Co/MCM-41 ones, where certain structure distortion can be caused by the partial collapse as well as the block of the some mesostructured pores [26]. Fig. 2 shows the high-angle XRD patterns for all of the calcined samples. For both Cr loadings, diffraction lines at $2\theta = 24.6$, 33.8, 36.4, 41.7, 50.6, 55.2, 63.9, 65.6 and 73.5°, corresponding to the crystalline phase of α-Cr_2O_3, were detected [31]. The estimated mean crystallite sizes were 48 ± 6 and 63 ± 9 nm for the low and high Cr content, respectively. The lack of XRD peaks assignable to crystalline iron oxides for the Fe-modified samples, suggests that these oxides, if exists, are in amorphous state or are clusters/particles too small to be detected by XRD. Meanwhile, for both Co contents, the samples exhibit small peaks at $2\theta = 36.8$, 44.8, 59.3 and 65.2° characteristic of Co_3O_4 nano-particles, which have an estimated mean crystallite size of 9 ± 3 nm. In the case of the TiO_2 loaded samples (Fig. 2B), the diffraction lines emerging at $2\theta = 25$, 37, 48, 54, 55 and 63° indicate the presence of the anatase crystalline phase [32], with an estimated mean crystallite size of around 29 ± 4 nm. It is noteworthy that although large oxides particles (Cr_2O_3, Co_3O_4 or TiO_2) on the external surface were detected by XRD, this fact does not allow us to discard the existence of different metal species linked or highly dispersed inside the mesoporous channels.

The results obtained by N_2 adsorption/desorption isotherms (not shown), for all of the calcined samples and other physical parameters are collected in Table 1. All of the samples exhibit type IV isotherms [29], typical of well-defined mesoporous structures with an inflection at relative pressure $P/P_0 \approx 0.1$–0.25 characteristic of capillary condensation inside the mesopores in the MCM-41 structure. Judging by this inflection, whereas the samples loaded with both contents of Cr, Fe, Co or only titania show a narrowly defined pore diameter range, when TiO_2 is loaded on the TM/MCM-41 samples the pore size distribution becomes broader, mainly for the higher TM loading. This is besides giving account for a lower structural order according to the XRD results. All the materials exhibit high surface area and high pore volume typical of MCM-41 type materials (Table 1). The metal-modified samples, in comparison with MCM-41, exhibit a decrease in the values of the surface area and the pore volume, probably due to the presence of clusters and/or small particles of metal oxides finely dispersed inside the channels as well as large particles (detectable by XRD) on the external surface, which could affect the pore structure. This feature is principally notable for the higher TM content and when titania is deposited on the TM/MCM-41 samples [23]. It is noteworthy that the molecular sieves synthesized by us have wall thicknesses much larger than that of the typical MCM-41 materials (Table 1) [33,34], which would possibly confer greater stability to the catalyst. On the other hand, comparing the Cr-modified samples, only the sample prepared with the higher Cr content showed a light increase in the wall thickness with respect to MCM-41, which is giving account for the major presence of different chromium species finally dispersed inside the channels [33,35–37]. When TiO_2 was loaded on the samples, only TiO_2/Cr–MCM-41(5) showed a light thickening of the pore wall, which could indicate that the lower content of chromium species allow the easier diffusion of the titanium species into the channels. Instead, the titanium species could not enter inside the pores of Cr–MCM-41(10), possibly due to the higher content of small size Cr-species on the channels surface and large α-Cr_2O_3 particles that could block the pores. For the Fe-modified samples, the metal species finely dispersed inside the channels and the absence of large particles of iron oxides could promote the formation of titania species inside the channels, leading to a pore wall thickening under the TiO_2 loading. Meanwhile, the cobalt seems to promote the growth of oxides particles on the external surface of the samples, causing high structure deterioration. Only Co/MCM-

Table 1
Chemical composition, textural and structural properties of the calcined materials.

Sample	Ti[a] (wt.%)	Cr[b] (wt.%)	Fe[b] (wt.%)	Co[b] (wt.%)	Area (m^2/g)	V_p (cm^3/g)	D_p[c] (Å)	t_w[d] (Å)
MCM-41	–	–	–	–	1182	1.15	27.0	14.9
Cr/MCM-41(5)	–	4.500	–	–	1045	0.84	26.3	14.5
Cr/MCM-41(10)	–	8.825	–	–	1006	0.83	25.4	16.2
Fe/MCM-41(5)	–	–	4.590	–	997	0.80	25.2	14.4
Fe/MCM-41(10)	–	–	8.010	–	886	0.75	26.1	14.9
Co/MCM-41(5)	–	–	–	5.400	1021	0.81	25.4	16.4
Co/MCM-41(10)	–	–	–	9.954	945	0.79	26.2	14.7
TiO_2/MCM-41	15.137	–	–	–	849	0.80	26.0	14.8
TiO_2/Cr/MCM-41(5)	14.850	2.880	–	–	791	0.45	23.2	15.9
TiO_2/Cr/MCM-41(10)	14.670	4.500	–	–	706	0.54	24.6	16.4
TiO_2/Fe/MCM-41(5)	12.960	–	2.655	–	773	0.28	21.7	17.7
TiO_2/Fe/MCM-41(10)	14.940	–	5.850	–	608	0.34	21.8	17.6
TiO_2/Co/MCM-41(5)	15.900	–	–	5.400	651	0.55	25.5	12.3
TiO_2/Co/MCM-41(10)	15.498	–	–	7.083	596	0.51	26.1	13.7

[a] Measured by ICP-AES.
[b] Measured by AA.
[c] Pore diameter corresponding to the maximum of the pore distribution obtained by the BJH method.
[d] $t_w = a_0 - D_p$.

41(5) seems to give account for the presence of finally dispersed Co species inside channels, judging by the pore wall thickness slightly increased with respect to that of MCM-41. Finally, the presence of titania species linked to the internal surface of all of these materials can be considered although titania particles growth on the external surface, as it is evidenced by XRD.

To get an insight into the coordination geometry and the position of the TM in our samples, diffuse reflectance spectra of the calcined samples were recorded as presented in Fig. 3. The Cr-modified samples show absorptions characteristic of Cr(VI) in tetrahedral coordination at 200 nm and 370 nm corresponding to the charge transfer from $O^{2-} \rightarrow Cr^{6+}$ due to monochromate species [$(CrO_4)^{2-}$] [21,38–40] and between 400 and 550 nm attributed to Cr^{6+} species in di/polychromates. Moreover, the absorption of octahedral Cr^{3+} in small Cr_2O_3 particles or clusters must also be considered in the last region [11,26,41,42]. Therefore, at this wavelength range (400–550 nm), the overlapping of absorptions due to both Cr^{6+} and Cr^{3+} species is highly probable. Moreover, the possible absorption of octahedral Cr^{3+} in small Cr_2O_3 particles or clusters [15,26,41,43,44] should be also considered in this region, since that quantum size effects induced by the decrease in the particle size lead to a blue shifted spectral response [42]. Meanwhile, the absorption that appears around 600 nm, principally in Cr/MCM-41(10), is assigned to Cr(III) species in octahedral coordination present in α-Cr_2O_3 nano-particles, which were already observed by XRD [38,39]. It is known that when the Cr^{3+} species are calcined in air after the impregnation process, higher valence species appear. Thus, depending on the loading degree, the chromium can be stabilized in the hexavalent state until certain saturation coverage of the support surface is reached [14,31,44,45]. Beyond this limit, the calcination process results insufficient and the complete oxidation of Cr^{3+} to Cr^{6+} cannot be achieved, leading to the formation of Cr_2O_3 clusters and/or α-Cr_2O_3 nano-particles responsible of the absorption at longer wavelengths. That is the reason why when the chromium loading was duplicated (Cr/MCM-41(10)) an increase in the absorption around 450 nm and the appearance of an intense band at 600 nm were observed. In addition, taking account that the surface composition influences the color of the supported catalyst, the dark yellow color for Cr/MCM-41(5) and the dark green color for Cr/MCM-41(10) constitute a further evidence for the dominant presence of Cr^{6+} (yellow) and Cr^{3+} (green) species, respectively. With respect to the TiO_2/Cr/MCM-41 samples, its spectrum resembles to that of the TiO_2/MCM-41 sample in the UV region, although it is observed an increase in the absorption in the 300–400 range, probably due to the absorption of monochromate species [11,26,41]. Then, these samples also show absorptions at about 400–550 and 550–750 nm related to the mentioned Cr species. It is notable, principally for the TiO_2/Cr/MCM-41(10), that those maxima corresponding to Cr^{6+} overlap, resulting in a unique absorption. Some authors related the coincidence of bands between TiO_2 and chromate species in the 370–500 nm range to a heterojunction of titania and chromium species [21]. In this sense, Di Iorio et al. [46] have reported spectroscopic evidence of a charge-transfer complex between TiO_2 and Cr^{6+} which is responsible for an absorption at 375 nm. Finally, it is clear that the ability to absorb visible light for the TiO_2/Cr/MCM-41 samples is highly related to the Cr presence [47]. Meanwhile, for the spectra corresponding to the Fe/MCM-41 samples three absorption regions at about 200–310 nm, 310–450 and 450–650 nm can be considered [48]. The first, associated with the dπ–pπ charge transfer between Fe and O [49], indicates that some iron atoms are able to link to O atoms, being incorporated into the matrix framework as isolated Fe^{3+} cations. The contributions detected at longer wavelengths evidence that iron is also present with octahedral coordination in extra-framework positions as small oligonuclear $(FeO)_n$ clusters [49–51] and/or very small iron oxide nano-particles (probably Fe_2O_3) [51]. When the iron loading was duplicated a slight increase

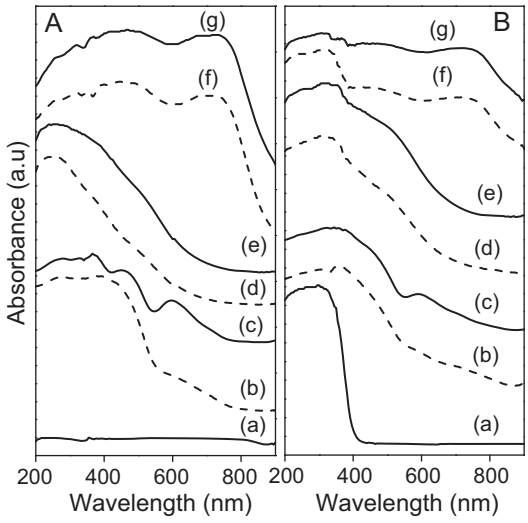

Fig. 3. UV–Vis DRS spectra, performed in absorbance mode, of the (A) – (a) MCM-41, (b) Cr/MCM-41(5), (c) Cr/MCM-41(10), (d) Fe/MCM-41(5), (e) Fe/MCM-41(10), (f) Co/MCM-41(5), (g) Co/MCM-41(10); (B) – (a) TiO_2/MCM-41, (b) TiO_2/Cr/MCM-41(5), (c) TiO_2/Cr/MCM-41(10), (d) TiO_2/Fe/MCM-41(5), (e) TiO_2/Fe/MCM-41(10), (f) TiO_2/Co/MCM-41(5), (g) TiO_2/Co/MCM-41(10).

in the absorption range between 300 nm and 600 nm allow us to realize about the higher presence of $(FeO)_n$ clusters and oxide nanoparticles, even if, due to their small size, they are not detectable by XRD [33,52]. In the case of the TiO_2/Fe/MCM-41 samples, besides the UV absorbance feature corresponding to TiO_2, it is possible to observe a slight increase in the absorption in the visible region with respect to the Fe/MCM/41 samples, likely due to a heterojunction effect between TiO_2 and iron species. For the Co/MCM-41 samples, the absorption between 200 and 300 nm is assigned to the charge transfer between the oxygen and Co^{2+} ion in tetrahedral symmetry [53,54]; meanwhile, the maxima at 300 and 400 nm are assigned to electronic transitions of Co^{3+} in disordered tetrahedral environment [54–56]. On the other hand, the absorption in the range 400–600 nm is assigned to octahedral Co^{2+} species, such as CoO clusters and the absorption between 600 and 800 nm indicates the presence of cobalt oxide nano-particles (Co_3O_4) where Co^{2+} ions are in tetrahedral coordination and Co^{3+} ions are in octahedral positions [53,57,58]. In the case of the TiO_2/Co/MCM-41 samples, the absorption feature in the visible region is very similar to that of the Co/MCM-41 samples, showing no evidence of heterojunction between titania and Co species. Finally, even though all the materials modified with transition metals absorb in the visible range, it is necessary to consider that the absorption of long wavelength light by the catalyst is a necessary condition for their photo-activity in visible light, but it is not sufficient to perform as an efficient photo-catalyst [11].

The TPR profiles of the calcined catalysts are presented in Fig. 4. The reducibility of metal species has been a useful means for detecting the interactions between the metal and the support [26,59]. Since TPR is a bulky process, not all particles are exposed to hydrogen at the same time producing a dependence of the temperature maximum on the particle size. For bulky oxides is expected an increase in the temperature maximum with the particle size. However, metal oxides loaded or incorporated in inert supports may exhibit different reduction behaviors compared with the metal oxides unsupported. In this sense, the TPR profile of metal oxides supported on inert matrixes such as MCM-41 are in general more complex than that of bulky metal oxides because there exists a wide range of variables including the particle size of the metal oxide and its interaction with the matrix. It is known that a decrease in the size of the metal oxide particles makes the reduction faster due to a higher surface area/volume ratio while smaller particles interact more intensely with the support and slow down the reduction. Therefore, the reducibility of the materials would be the result of the competition of these two factors [37]. With respect to the Cr-loaded samples (Fig. 4A), one single reduction band centered at 550 °C, due to the reduction of Cr^{6+} to Cr^{3+} ions [59,60], was observed for the Cr/MCM-41(5) sample. When the Cr loading was duplicated for the Cr/MCM-41(10) sample, this reduction temperature decreased emerging two hydrogen consumptions at 350 °C and 490 °C, usually assigned to Cr^{6+} species with different interactions with the support [52,61]. These hydrogen consumption could probably be associated with the reduction of di/poly-chromates and monochromate species like $(CrO_4)^{2-}$, already observed by UVvis-DRS [40,62,63]. The only peak at high temperature present in the Cr/MCM-41(5) sample profile is given account for the predominance of Cr(VI) species as monochromates of high interaction with the support. This fact would be a consequence of the higher dispersion of these species due to the low Cr content [31,59]. Moreover, for the Cr/MCM-41(10) sample, two additional hydrogen consumptions appear: one at 250 °C assigned to the reduction of Cr^{6+} species dispersed on α-Cr_2O_3 [64] and other at 600–800 °C assigned to the reduction of Cr^{3+}, also ascribed to the presence of crystalline α-Cr_2O_3 [31,65]. Given the high Cr loading in this material, the silanol groups on the MCM-41 surface are not able to stabilize the Cr^{6+} species and the hydrogen consumption at high

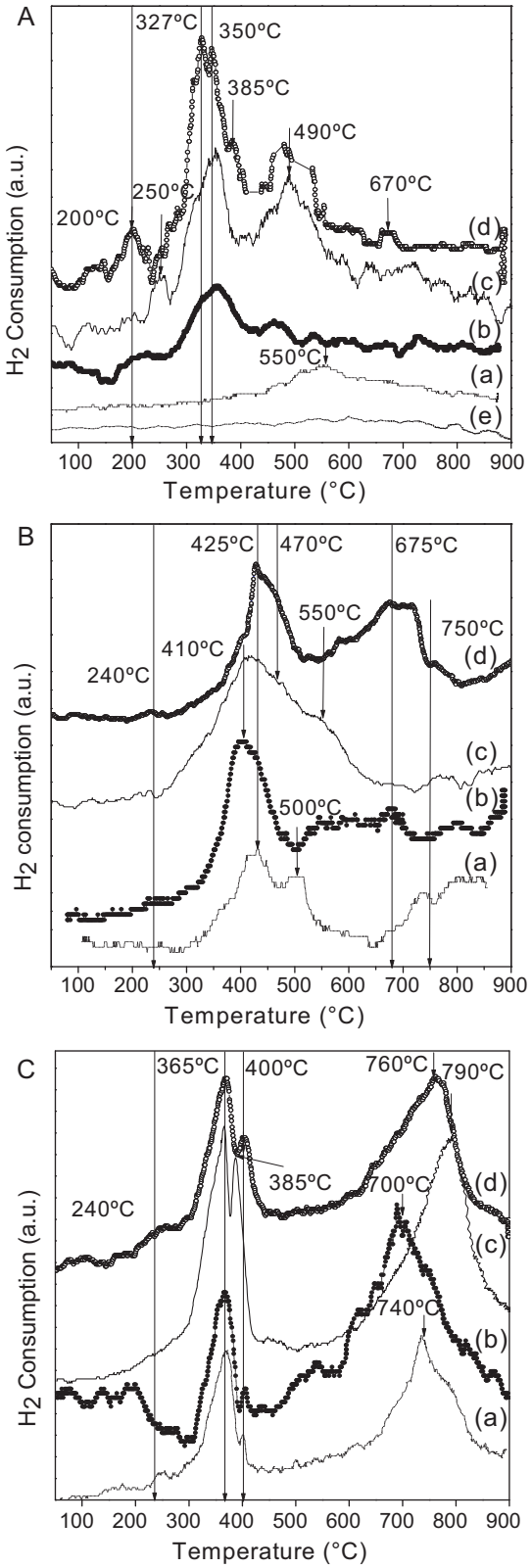

Fig. 4. TPR profiles of (A) – (a) Cr/MCM-41(5), (b) TiO_2/Cr/MCM-41(5), (c) Cr/MCM-41(10),(d) TiO_2/Cr/MCM-41(10), (e) TiO_2/MCM-41; (B) – (a) Fe/MCM-41(5), (b) TiO_2/Fe/MCM-41(5), (c) Fe/MCM-41(10), (d) TiO_2/Fe/MCM-41(10); (C) – (a) Co/MCM-41(5), (b) TiO_2/Co/MCM-41(5), (c) Co/MCM-41(10), (d) TiO_2/Co/MCM-41(10).

temperature would be giving account for the presence of Cr_2O_3 particles [14]. Based on these results we can conclude that, in both samples, the Cr mainly exists in 6+ oxidation state (mono and di/polychromates), but the chromium loading increasing leads to the increased formation of Cr^{+3} in octahedral coordination. This fact is according with the UV–Vis DRS and XRD results that indicate the lower presence of α-Cr_2O_3 particles of smaller size for the Cr/MCM-41(5) sample. The TiO_2/Cr/MCM-41 samples present new reduction peaks at 200 and 327 °C, which can be attributed to the dehydroxylation of TiO_2 surface [11] and to the reduction of Cr^{6+} to Cr^{5+} due to the interaction between Cr and TiO_2 [18], respectively. This Cr^{+5} specie is hardly further reduced due to their covering by the titania, avoiding the completely reduction to Cr^{3+}. In particular, the TiO_2/Cr/MCM-41(10) sample shows an additional hydrogen consumption at 670 °C which is usually assigned to the reduction of Ti^{4+} to Ti^{3+}, promoted by the interaction with Cr species [26,66]. Moreover, it is worth to note that the hydrogen consumption at high temperature, corresponding to Cr_2O_3, is reduced with respect to the Cr/MCM-41(10) sample, probably due to their stabilization in the MCM-41 structure by their covering with TiO_2. The TPR profiles of the Fe/MCM-41 samples allow us to estimate the reducibility of the iron species for both loadings (Fig. 4B). For the lower Fe loading, two well-resolved TPR peaks appear at 425 and 500 °C. These can be related to $Fe_2O_3 \rightarrow Fe_3O_4$ and $Fe_3O_4 \rightarrow FeO$ processes, respectively. On the other hand, the hydrogen consumption at temperatures higher than 700 °C can be ascribed to framework Fe^{3+} species of difficult reducibility [67]. This high reduction temperature is indicative of the shielding effect of the mesoporous framework, which protects the isolated Fe^{3+} cations from H_2 attack [67]. Therefore, at this low iron content, the Fe^{3+} species are reduced, even at high temperatures, only to Fe^{2+} species, which are stabilized in the MCM-41 structure with high resistance to the reduction to metallic state. Meanwhile, for the Fe/MCM-41(10) sample three peaks emerge at 410, 470 and 550 °C. The two first temperatures are associated with the reduction process already explained, and the third one is assigned to the $FeO \rightarrow Fe^0$ process [68]. Therefore, the complete reduction of iron oxide species to the zero-valence state can be reached due to the high loading of iron (8 wt%), which makes easier the further reduction of ferrous cations. This phenomenon was already observed for iron supported on silica [69,70]. It should be noted that the bulk iron oxide can be reduced to the zero-valence state at 400 °C [71]. In addition, the smaller hydrogen consumption above 700 °C indicates the lower reduction of isolated Fe^{3+} species, less accessible. With respect to the TiO_2/Fe/MCM-41(5) sample, the peak at 500 °C present in Fe/MCM-41(5) disappears, indicating that the complete reduction to Fe^{2+} does not occur. Meanwhile, the disappearance of the peak at 550 °C, present in Fe/MCM-41(10), for the TiO_2/Fe/MCM-41(10) sample is indicating that Fe^{2+} is not completely reduced to Fe^0. Thus, in both cases, the iron species would be protected of a further reduction through the covering by the TiO_2. Furthermore, for both iron contents, two new reduction temperatures appear at 240 °C and 675 °C, which can be awarded to the dehydroxylation of the TiO_2 surface [11] and to the reduction of Ti^{4+} to Ti^{3+} [16,50], respectively. Although it is known that TiO_2 is reduced at very high temperatures (around 1300 °C) [72], Fe_2O_3 may promote the reduction of Ti^{4+} ions, which leads to a shift of the reduction peak of TiO_2 to lower temperature [66]. The higher hydrogen consumption around 675 °C for the TiO_2/Fe/MCM-41(10) sample is produced by the easier reduction of Ti^{4+} to Ti^{3+}, probably promoted by the higher iron content. For the Co/MCM-41 samples (Fig. 4C) two reduction regions could be distinguished: one at low-temperature (LT) and one at high-temperature (HT) which can be ascribed to the reduction of metal oxide species with different dispersion and different interaction with the support. A first doublet that appears in the temperature range 300–400 °C may be attributed to the Co_3O_4 supported crystallites that interacts weekly with the surface and are not well dispersed on it, giving rise to reduction at lower temperature [55,73]. It is well known that reduction of Co_3O_4 takes place in two steps: the first reduction peak corresponds to the following process: $Co_3O_4 \rightarrow CoO$, while the second one corresponds to $CoO \rightarrow Co^0$ transition. On the other hand, the intense peak in the HT region can be attributed to Co^{3+} and Co^{2+} species, probably present in very small supported Co_3O_4 crystallites that are finely dispersed and interacts strongly with the surface, resulting in its reduction at higher temperatures. For the Co/MCM-41(10) sample, the shift of the second peak to lower temperatures (385 °C) with respect to that of Co/MCM-41(5) indicates a lower interaction of the not well-dispersed Co_3O_4 particles with the support when the Co loading is increased. Meanwhile, the shift to higher temperatures (790 °C) for the peak in the HT region would indicate a higher interaction of the smaller particles highly dispersed, when the Co loading is increased. For the TiO_2/Co/MCM-41 samples, one can clearly observe in its TPR profiles a shoulder at lower temperature besides the three reduction peaks corresponding to the different Co species just mentioned for the samples Co/MCM-41. This shoulder around 200 °C is assigned again to the dehydroxylation of TiO_2 surface. Moreover, comparing to the samples without TiO_2, the shift to lower temperatures for the peak in the HT region could suggest the reduction of Ti^{4+} to Ti^{3+}, which would appear overlapped to the reduction corresponding to the Co species. Finally, according to the literature [26], both the dehydroxylation of TiO_2 surface and the reduction of Ti^{4+} to Ti^{3+}, not present in the TiO_2/MCM-41 sample, would make evident some kind of interaction between metal and titania species for all of the TiO_2/TM/MCM-41 samples.

3.2. Photocatalytic evaluation

Considering the photo-degradation tests, experiments without catalyst and in the dark were previously carried out. Without catalyst, no appreciable photo-degradation was observed during 5 h of UV–Vis and visible irradiation (about 10% and 2%, respectively). In the dark, certain decrease of AO7 (about 25.00%, 2.50% and 3.50% for the Cr-, Fe- and Co-modified samples, respectively) took place after 45 min of continuous stirring due to the adsorption phenomena. Meanwhile, no photocatalytic activity was observed for the bare MCM-41. It is known that the photo-catalytic degradation rate (r) of azo-dyes over illuminated TiO_2 fitted the Langmuir–Hinshelwood (L–H) kinetics model [2]. When C_0 is small the equation can be simplified to an apparent first-order equation: $\ln(C_0/C) = k_{app} \times t$, where t is the illumination time and k_{app} the apparent first-order rate constant. It is noteworthy that the rate constant calculated is not regarded as fully interpretable, but it simply serves to compare relative activities of the catalyst under study. Table 2 lists the AO7 degradation percentage (X) at a reaction time of 5 h and the calculated k_{app} values. Under visible radiation TiO_2/MCM-41 sample showed an activity around 10%. This is attributed by some authors to a photo-induced process by photo-absorption of dye itself, in which dyes are excited by absorbing visible light photons and immediately inject electrons into the TiO_2 conduction band with initiating the degradation of dyes [74–76]. Among all the TM/MCM-41 samples, the Cr-modified materials presented the highest AO7 degradation percentages and the highest k_{app} values. This high photo-activity would be related with the presence of tetrahedral coordinated Cr^{6+} ions highly dispersed on the internal surface of the MCM-41 structure [77]. Under this radiation a special transition: $Cr^{6+}–O^{2-} \rightarrow Cr^{5+}–O^{1-}$ is possible. This charge-transfer excited state has high reactivity due to the presence of electron–hole pairs localized next to each other. These pairs can interact with surface hydroxyl groups on MCM-41 or adsorbed oxygen to produce highly reactive radical species which can ini-

Table 2
Apparent rate constants (k_{app}) and degradation percentage for the AO7 under UV–Vis and visible radiation at 5 h. The experimental conditions were air-equilibrated; pH 5; [AO7] = 20 ppm; [catalyst] = 1 g/L.

Catalyst	Visible radiation			UV–Vis radiation		
	X[a] $(C_0 - C_f/C_0) \times 100$	k_{app} (min^{-1})	R^2	X[a] $(C_0 - C_f/C_0) \times 100$	k_{app} (min^{-1})	R^2
Cr/MCM-41(5)	69.29 (±0.09)	0.175	0.973	89.83 (±0.08)	0.633	0.957
Cr/MCM-41(10)	80.95 (±0.08)	0.314	0.994	87.58 (±0.08)	0.545	0.959
Fe/MCM-41(5)	1.79 (±0.09)	–	–	9.78 (±0.09)	0.027	0.988
Fe/MCM-41(10)	0.89 (±0.09)	–	–	10.05 (±0.09)	0.020	0.923
Co/MCM-41(5)	0.00 (±0.09)	–	–	5.06 (±0.09)	0.016	0.994
Co/MCM-41(10)	1.75 (±0.09)	–	–	6.61 (±0.09)	0.019	0.990
TiO_2/MCM-41	9.50 (±0.08)	0.022	0.962	51.25 (±0.10)	0.167	0.985
TiO_2/Cr/MCM-41(5)	66.52 (±0.08)	0.271	0.981	95.68 (±0.08)	0.785	0.975
TiO_2/Cr/MCM-41(10)	79.37 (±0.12)	0.305	0.999	98.65 (±0.07)	0.932	0.958
TiO_2/Fe/MCM-41(5)	10.21 (±0.09)	0.031	0.938	54.94 (±0.1)	0.189	0.964
TiO_2/Fe/MCM-41(10)	12.61 (±0.09)	0.034	0.968	54.39 (±0.10)	0.181	0.963
TiO_2/Co/MCM-41(5)	4.69 (±0.09)	0.016	0.985	40.63 (±0.10)	0.125	0.981
TiO_2/Co/MCM-41(10)	5.13 (±0.09)	0.015	0.957	36.47 (±0.10)	0.106	0.961

[a] The confidence limit for the degradation percentage for a 95% of confidence, are given in parentheses.

tiate the photo-catalytic degradation. Nevertheless, when the Cr content was duplicated the degradation reached a maximum of 81%. This low increment in the photo-activity could be associated with the higher presence of Cr^{3+} species on the Cr/MCM-41(10) sample. Thus, this result gives evidence about that the Cr^{6+} is the photo-active specie. In contrast to that we expected, an increase in the photo-activity, due to a sensitization of titania with Cr^{6+} species, could not be observed after the TiO_2 loading. As it has been explained, when the Cr content is higher than the saturation coverage of the support surface, Cr^{3+} species as Cr_2O_3 clusters and/or α-Cr_2O_3 nano-particles start to appear, which could be avoiding the desired heterojunction effect between the Cr^{6+} and titania species. Meanwhile, the TiO_2 loading on the Fe-modified samples resulted in a slightly incremented photo-activity with respect to the TiO_2/MCM-41 giving account for certain heterojunction effect between the iron and titania species. This could be explained by the presence of Fe^{3+} ions acting as shallow charge trapping sites which partially prevent the recombination process of electron/holes pairs [78,79]. On the other hand, the poor activity of the TiO_2/Co/MCM-41 samples could be related to the presence of Co, which hinders the photo-activity exhibited by the TiO_2/MCM-41 sample. Probably, this metal can accelerate the recombination of photoexcited electrons and holes acting as a recombination center. Under UV–Vis radiation, for all of the tested catalysts, the degradation was higher than when visible radiation was used. This fact can be attributed to the higher radiation that reaches the suspension. The TiO_2/MCM-41 sample showed a dye degradation of 51%, while using the same TiO_2 Degussa P-25 concentration (1 g/L), a degradation of 90% was reached (not shown). Taking into account that the Ti content in TiO_2/MCM-41 is much lower than that in commercial TiO_2, it can be thought that the Ti in the former catalyst acts as a more active photo-catalytic site. This behavior could be due to the higher dispersion of Ti on the mesoporous structure as compared with commercial TiO_2 [30]. The high k_{app} values obtained for the Cr/MCM-41 catalysts are giving account for the high photo-catalytic activity of chromium itself, although the variation of Cr content has not affected the final degradation of AO7. Nonetheless, when TiO_2 was loaded on these materials an almost total degradation of the AO7 (higher than 95%) was reached. This fact can be due to the additional activity of Ti itself under UV radiation. Meanwhile, the TiO_2/Fe/MCM-41 samples presented practically the same activity that the TiO_2/MCM-41, indicating that the iron does not improve the activity of the Ti when UV radiation is used. On the other hand, it should be noted that the Co hindered the photo-activity exhibited by the TiO_2/MCM-41 sample, acting as an electron–hole recombination center.

4. Conclusions

Mesoporous molecular sieves were synthesized with two different loadings of Cr, Fe or Co and then modified with TiO_2. All of the materials exhibit good structural regularity retaining the MCM-41 structure after the metal incorporation. The photo-catalytic activity of all the catalysts under visible or UV–Vis light was tested for the AO7 degradation. Only the Cr-modified photo-catalysts showed high activity under visible radiation. The results of TPR and UV–Vis DRS characterization demonstrate that the Cr content in the samples has a significant effect on the oxidation state and the coordination of chromium species, indicating that the Cr^{3+} species are increased when the Cr loading increases. The lack of increment in the photo-activity when the Cr content was duplicated suggests that Cr^{6+} is the photo-active specie. Contrary to expectations, the loading of TiO_2 on the samples previously modified with Cr, did not present increment in the catalyst photo-activity. This result is attributed to the presence of Cr^{3+} species as Cr_2O_3 clusters and/or α-Cr_2O_3 nano-particles, which could be avoiding the desired heterojunction effect between the metal species. Finally, the degradation percentage reached with the Cr-modified catalysts using visible light is an important result, more even if we take account that the radiation available was approximately the 10% of the lamp radiation.

Acknowledgments

G.E., S.C., K.S. and M.O CONICET Researchers; V.E. and E.V. CONICET Doctoral Fellowships. This work was supported by the CONICET and UTN-FRC of Argentina. The authors are grateful to INTeC from UNL for the UV–Vis DRS spectra. We thank to Eng. Ema Sabre and Elisa Ortiz (engineering student) for their valuable help in experimental activities.

References

[1] A. Alinsafi, F. Evenou, E.M. Abdulkarim, M.N. Pons, O. Zahraa, A. Benhammou, A. Yaacoubi, A. Nejmeddine, Dyes Pigm. 74 (2007) 439–445.
[2] I. Konstantinou, T. Albanis, Appl. Catal. B 49 (2004) 1–14.
[3] D. Robert, S. Malato, Sci. Tot. Environ. 291 (2002) 85–97.
[4] M. Stylidi, D. Kondarides, X. Verykios, Appl. Catal. B 47 (2004) 189–201.
[5] C. Galindo, P. Jacques, A. Kalt, J. Photochem. Photobiol. A 130 (2000) 35–47.
[6] A. Aguedach, S. Brosillon, J. Morvan, E. Lhadi, Appl. Catal. B 57 (2005) 55–62.
[7] H. Zhang, D. Chen, X. Lv, Y. Wang, H. Chang, J. Li, Environ. Sci. Technol. 44 (2010) 1107–1111.
[8] A. Mills, J. Wang, D.F. Ollis, J. Catal. 243 (2006) 1–6.
[9] L. Lucarelli, V. Nadtochenko, J. Kiwi, Langmuir 16 (2000) 1102–1108.
[10] M. Satuf, R. Brandi, A. Cassano, O. Alfano, Ind. Eng. Chem. Res. 44 (2005) 6643–6649.

[11] L. Davydov, E. Reddy, P. France, P. Smirniotis, J. Catal. 203 (2001) 157–167.
[12] X. Chen, S. Shen, L. Guo, S.S. Mao, Chem. Rev. 110 (2010) 6503–6570.
[13] J. Wang, Z. Liu, R. Cai, Environ. Sci. Technol. 42 (2008) 5759–5764.
[14] S. Shylesh, C. Srilakshimi, A. Singh, B. Anderson, Micropor. Mesopor. Mater. 99 (2007) 334–344.
[15] Z. Liu, Z. Cui, Z. Zhang, Mater. Charac. 54 (2005) 123–129.
[16] R. Pozzo, M. Baltanás, A. Cassano, Catal. Today 39 (1997) 219–231.
[17] J. Beck, J. Vartuli, W. Roth, M. Leonowicz, C. Kresge, K. Schmidt, C. Chu, D. Olson, E. Sheppard, S. McCullen, J. Higgins, J. Schenkler, J. Am. Chem. Soc. 114 (1992) 10834–10843.
[18] P. Reddy, B. Sun, P. Smirniotis, J. Phys. Chem. B 108 (2004) 17198–17205.
[19] X. Wang, W. Lian, X. Fu, J.-M. Basset, F. Lefebvre, J. Catal. 238 (2006) 13–20.
[20] S. Higashimoto, Y. Hu, R. Tsumura, K. Iino, M. Matsuoka, H. Yamashita, Y. Gun Shul, M. Che, M. Anpo, J. Catal. 235 (2005) 272–278.
[21] F. Marques, M. Canela, A. Stumbo, Catal. Today 133–135 (2008) 594–599.
[22] S. Anandan, Dyes Pigm. 76 (2008) 535–541.
[23] S. Shen, L. Guo, Catal. Today 129 (2007) 414–420.
[24] M. Phanikrishna Sharma, V. Durga Kumari, M. Subrahmanyam, Chemosphere 72 (2008) 644–651.
[25] R. Van Grieken, J. Aguado, M. López-Muñoz, J. Marugán, J. Photochem. Photobiol. A 148 (2002) 315–322.
[26] B. Sun, E.P. Reddy, P.G. Smirniotis, Appl. Catal., B 57 (2005) 139–149.
[27] V. Elías, M. Crivello, E. Herrero, S. Casuscelli, G.A. Eimer, J. Non-Cryst. Solids 355 (2009) 1269–1273.
[28] A. Patterson, Phys. Rev. 56 (1939) 978–982.
[29] S. Gregg, K. Sing, Adsorption Surface Area and Porosity, Academic Press, 1982.
[30] Y. Do, J. Kim, J. Park, S. Park, S. Hong, C. Suh, G. Lee, Catal. Today 101 (2005) 299–305.
[31] L. Zhang, Y. Zhao, H. Dai, H. He, C.T. Au, Catal. Today 131 (2008) 42–54.
[32] S. Awate, N. Jacob, S. Deshpande, T. Gaydhankar, A. Belhekar, J. Mol. Catal. A 226 (2005) 149–154.
[33] C. Chanquía, K. Sapag, E. Rodriguez-Castellón, E. Herrero, G.A. Eimer, J. Phys. Chem. C 114 (2010) 1481–1490.
[34] G. Soller-Illia, C. Sanchez, B. Lebeau, J. Patarin, Chem. Rev. 102 (2002) 4093.
[35] A. Szegedi, Z. Kónya, D. Méhn, E. Solymár, G. Pál-Borbély, Z.E. Horváth, L.P. Biró, I. Kiricsi, App. Catal. A 272 (2004) 257–266.
[36] Z. Li, L. Gao, J. Phys. Chem. Sol. 64 (2003) 223–228.
[37] X. Hao, Y. Zhang, J. Wang, W. Zhou, C. Zhang, S. Liu, Micropor. Mesopor. Mater. 88 (2006) 38–47.
[38] S. Shylesh, P. Samuel, A.P. Sing, Appl. Catal. A 318 (2007) 128–136.
[39] M. Anpo, T. Kim, M. Matsuoka, Catal. Today 142 (2009) 114–124.
[40] B. Weckhuysen, I. Wachs, R. Schoonheydt, Chem. Rev. 96 (1996) 3327–3349.
[41] X. Fan, X. Chen, S. Zhu, Z. Li, T. Yu, J. Ye, Z. Zou, J. Mol. Catal. A 284 (2008) 155–160.
[42] D. Beydoun, R. Amal, G. Low, S. McEvoy, J. Nanoparticle Res. 1 (1999) 439–458.
[43] S. Rodrigues, S. Uma, I. Martyanov, K. Klabunde, J. Catal. 230 (2005) 158–165.
[44] Y. Ohishi, T. Kawabata, T. Shishido, K. Takaki, Q. Zhang, Y. Wang, K. Takehira, J. Mol. Catal. A 230 (2005) 49–58.
[45] L. Liu, H. Li, Y. Zhang, Catal. Commun. 8 (2007) 565–570.
[46] Y. DiIorio, E. San Román, M. Litter, M. Grela, J. Phys. Chem. C 112 (2008) 16532–16538.
[47] J. Pedraza-Avella, R. López, F. Martinez-Ortega, E. Páez-Mozo, R. Gómez, J. Nano Res. 5 (2009) 95–104.
[48] V. Elías, M. Oliva, S. Urreta, S. Silvetti, K. Sapag, A. Mudarra Navarro, S. Casuscelli, G. Eimer, Appl. Catal. A 381 (2010) 92–100.
[49] Y. Lu, J. Zheng, J. Liu, J. Mu, Micropor. Mesopor. Mater. 106 (2007) 28–34.
[50] Y. Wang, Q. Zhang, T. Shishido, K. Takehira, J. Catal. 209 (2002) 186–196.
[51] S. Liu, Q. Wang, P. Van Der Voort, P. Cool, E. Vansant, M. Jiang, J. Magn. Magn. Mater. 280 (2004) 31–36.
[52] A. Gaspar, L. Dieguez, Appl. Catal. A 227 (2002) 241–254.
[53] M. Karthik, A. Tripathi, N. Gupta, A. Vinu, M. Hartmann, M. Palanichamy, V. Murugesan, Appl. Catal. A 268 (2004) 139–149.
[54] T. Somanathan, A. Pandurangan, D. Sathiyamoorthy, J. Mol. Catal. A. 256 (2006) 193–199.
[55] S. Vetrivel, A. Pandurangan, J. Mol. Catal. A: Chem. 227 (2005) 269–278.
[56] S. Morpurgo, M. Lo Jacono, P. Porta, J. Solid State Chem. 122 (1996) 324–332.
[57] S. Bhoware, A. Singh, J. Mol. Catal. A: Chem. 266 (2007) 118–130.
[58] I. Zacharaki, C. Kontoyannis, S. Boghosian, A. Lycourghiotis, Ch. Kordulis, Catal. Today 143 (2009) 38–44.
[59] A. Gaspar, J. Brito, L. Dieguez, J. Mol. Catal. A 203 (2003) 251–266.
[60] K. Takehira, Y. Ohishi, T. Shishido, T. Kawabata, K. Takaki, Q. Zhang, Y. Wang, J. Catal. 224 (2004) 404–416.
[61] F. Cavani, M. Koutyrev, F. Trifiró, A. Bartolini, D. Ghisletti, R. Iezzi, A. Santucci, G. del Piero, J. Catal. 158 (1996) 236–250.
[62] X. Zhao, X. Wang, J. Mol. Catal. A 261 (2007) 225–231.
[63] Y. Wang, Y. Ohishi, T. Shishido, Q. Zhang, W. Yang, Q. Guo, H. Wan, K. Takehira, J. Catal. 220 (2003) 347–357.
[64] A. Hakuli, M. Harlin, L. Backman, A. Krause, J. Catal. 184 (1999) 349–356.
[65] G. Wang, L. Zhang, J. Deng, H. Dai, H. He, C. Au, App. Catal. A 355 (2009) 192–201.
[66] X. Li, B. Shen, C. Xu, Appl. Catal. A 375 (2010) 222–229.
[67] S. Bordiga, R. Buzzoni, F. Geobaldo, C. Lamberti, E. Giamello, A. Zecchina, G. Leofanti, G. Petrini, G. Tozzola, G. Vlaic, J. Catal. 158 (1996) 486–501.
[68] B. Coq, M. Mauvezin, G. Delahay, S. Kieger, J. Catal. 195 (2000) 298–303.
[69] H. Hayashi, L. Chen, T. Tago, M. Kishida, K. Wakabayashi, Appl. Catal. A 231 (2002) 81–89.
[70] P. Decyk, M. Trejda, M. Ziolek, J. Kujawa, K. Glaszczka, M. Bettahar, S. Monteverdi, M. Mercy, J. Catal. 219 (2003) 146–155.
[71] H. Topsøe, J.A. Dumesic, M. Boudart, J. Catal. 28 (1973) 477–488.
[72] M. Dewan, G. Zhang, O. Ostrovski, Metall. Mater. Trans. B 40 (2009) 62–69.
[73] S. Rodrigues, S. Uma, I. Martyanov, K. Klabunde, J. Photochem. Photobiol. A 165 (2004) 51–58.
[74] K. Vinodgopal, D. Wynkoop, Environ. Sci. Technol. 30 (1996) 1660–1666.
[75] X. Yan, T. Ohno, K. Nishijima, R. Abe, B. Ohtani, Chem. Phys. Lett. 429 (2006) 606–610.
[76] H. Kyung, J. Lee, W. Choi, Environ. Sci. Technol. 39 (2005) 2376–2382.
[77] S. Rodrigues, K. Ranjit, S. Uma, I. Martyanov, K. Klabunde, J. Catal. 230 (2005) 158–165.
[78] C. Wang, D. Bahnemann, J. Dohrmann, Chem. Commun. (2000) 1539–1540.
[79] M. Litter, J. Navío, J. Photochem. Photobiol. A 98 (1996) 171–181.